Physics of Plasmas ARTICLE pubs.aip.org/aip/pop

Electrostatic *full-f* gyrokinetic simulation of microturbulence in tokamak using canonical Maxwellian distribution

Cite as: Phys. Plasmas **33**, 102305 (2026); doi: 10.1063/5.0332067
Submitted: 2 March 2026 · Accepted: 2 October 2026 ·
Published Online: 29 October 2026

View Online Export Citation CrossMark

Haotian Chen,[1,2,a)] Pengfei Liu,[3,b)] Xishuo Wei,[2] and Zhihong Lin[4]

AFFILIATIONS

[1]Fusion Simulation Center, Peking University, Beijing 100871, China
[2]Honghu Future Energy (Shanghai) Ltd., Shanghai, China
[3]Institute of Physics, Chinese Academy of Sciences, Beijing 100190, China
[4]Galaxy Energy LLC, Irvine, California 92612, USA

[a)]Author to whom correspondence should be addressed: 2101110150@stu.pku.edu.cn
[b)]Electronic mail: pfliu@iphy.ac.cn

ABSTRACT

Electrostatic *full-f* global gyrokinetic simulations using a canonical Maxwellian distribution find that ion temperature gradient turbulence in a tokamak exhibits a transition after which the transport level decreases until the system reaches a steady state. The transport coefficient exhibits Bohm-like scaling before the transition and gyro-Bohm scaling after the transition, with a reduction of the transport level due to the interaction between drift wave turbulence and zonal flows. This transition is associated with the long-time evolution of the distribution function toward a nonlinear steady state consistent with the turbulence. In the steady-state turbulence, the $\mathbf{E} \times \mathbf{B}$ staircases form and exhibit quasi-regular long-lived meso-scale structures that regularize the turbulence.

© 2026 Author(s). All article content, except where otherwise noted, is licensed under a Creative Commons Attribution (CC BY) license (https://creativecommons.org/licenses/by/4.0/). https://doi.org/10.1063/5.0332067

03 November 2026 18:38:41

I. INTRODUCTION

Investigating turbulence and associated transport in toroidal plasmas is a crucial area of research in magnetic fusion. Gyrokinetic simulation[1] is a powerful tool in understanding turbulence and related nonlinear physics in fusion plasma. The gyrokinetic simulation method based on the low-noise perturbative algorithm (δf simulation) has become a crucial tool in the study of pressure-gradient-driven microinstabilities, including ion temperature gradient (ITG) instability, which plays an important role in turbulent transport processes in tokamaks.[2,3]

In the perturbative δf simulations, the system relaxes from linearly unstable initial conditions to a nonlinearly saturated marginal state. This paradigm complicates reliable estimation of steady transport levels under flux-driven conditions. Moreover, the δf method is not suitable for long-time simulations—up to energy-confinement or realistic collisional timescales in reactor-relevant regimes due to the accumulating particle noise.[4]

To address these limitations, non-perturbative *full-f* simulation schemes have been developed in some gyrokinetic codes.[4–8] In the *full-f* gyrokinetic particle simulations, the particle distribution function is solved self-consistently without assuming any scale separation. This approach enables the study of some important issues in tokamaks, such as the L-H transition, H-mode profile stiffness, and the effects of non-equilibrium distributions on turbulence dynamics. Full-f simulations also open new avenues for more realistic models of turbulence in the presence of realistic heat and/or particle sources.[4–7] In the collisionless *full-f* simulations,[9,10] it is crucial to use a distribution function in the constant of motion (COM) phase space as the initial distribution, such as the canonical Maxwellian (CM) distribution,[4,8,9,11] which is the exact equilibrium solution of the collisionless gyrokinetic equation in the axisymmetric toroidal devices.[12] The three COMs are canonical toroidal angular momentum ($\boldsymbol{P}_\zeta$), magnetic moment ($\boldsymbol{\mu}$), and total energy ($\boldsymbol{E}$). The local Maxwellian (LM) distribution, which is often used as an approximation in small orbit width limits, can produce spurious initial electric fields that can greatly affect the simulation results. However, it is usually difficult to customize the radial temperature and density profiles when initializing particles as a non-local CM.

In this paper, we present the results of global gyrokinetic simulations of electrostatic ITG turbulence using *full-f* simulation schemes

© Author(s) 2026

in the GTC code based on CM. We present a novel method to obtain the form of the CM by using two layers of iteration, and the resulting distribution has almost the same radial profile as the equilibrium radial profile, with a difference on the order of 0.1%. This iteration method for particle initialization enables us to do both δf and *full-f* simulations with CM distribution with the same radial profiles of density and temperature. We compare the results of using CM ($\boldsymbol{F_{CoM}}$) and LM ($\boldsymbol{F_{LM}}$) as the initial particle distribution. The result shows that in the *full-f* simulation, larger initial zonal flow oscillations are observed when using the LM. To further eliminate the initial perturbation and extend the linear growth stage in the *full-f* simulation, we perform nonlinear simulations starting from the steady-state CM distribution achieved after a pre-conditioning Monte Carlo simulation. The results of using CM show more consistent linear growth rates with the δf simulation results. This is attributed to the smaller profile gradient change in the Monte Carlo simulation when using the CM.[8]

In the long-time *full-f* simulation, a transition behavior of turbulent transport is found. Before the transition, the turbulence has high amplitude and exhibits avalanche type behavior[13,14] with multiple burst activities. Meanwhile, clear inward zonal flow propagation is observed. After the transition, the turbulence drops to a low amplitude, and zonal flow is dominated by zero-frequency zonal flow. From simulations with different equilibrium profiles and collision frequencies, we find that the transport coefficient exhibits Bohm-like[15] scaling before the transition and gyro-Bohm scaling after the transition. This reduction of transport level is likely due to the interaction between drift wave turbulence and zonal flows. Before the transition, the Doppler frequency associated with the radial propagation reduces the efficiency of the zonal flows' effect on turbulence.[16] After the transition, the inward propagation of zonal flows becomes weaker, and the turbulence is more effectively suppressed by the zero-frequency zonal flow. This transition is due to the evolution of the equilibrium distribution function toward a nonlinear steady state consistent with the turbulence. Similar turbulence and zonal flow behavior is also observed in gyrokinetic simulations[13,17–20] and a prey–predator reduced model.[21,22] In the steady-state turbulence, the $\mathbf{E}\times\mathbf{B}$ staircases[17] form and exhibit long-lived meso-scale structures, which suppress the turbulence. The scaling of $\mathbf{E}\times\mathbf{B}$ staircases with the equilibrium profile is also presented.

II. FULL-F SIMULATION MODEL

A. Electrostatic gyrokinetic simulation model

In the present study, we consider the electrostatic ITG turbulence described by gyrokinetic ions and adiabatic electrons in an axisymmetric toroidal configuration. In the modern gyrokinetic theory, the gyrokinetic Vlasov equation is written using the gyrocenter position $\mathbf{X}$, magnetic moment μ, and parallel velocity $v_\parallel$ as a set of independent variables in the five-dimensional phase space,[23,24]

$$\mathcal{L}f=\frac{d}{dt}f(\mathbf{X},\mu,v_\parallel,t)=\left(\frac{\partial}{\partial t}+\dot{\mathbf{X}}\cdot\nabla+\dot{v}_\parallel\frac{\partial}{\partial v_\parallel}-C\right)f=0, \tag{1}$$

$$\dot{\mathbf{X}}=v_\parallel\frac{\mathbf{B}^*}{B_\parallel^*}+\mathbf{v}_E+\mathbf{v}_g, \tag{2}$$

$$\dot{v_\parallel}=-\frac{1}{m}\frac{\mathbf{B}^*}{B_\parallel^*}\cdot(\mu\nabla B_0+Z\nabla\langle\phi\rangle). \tag{3}$$

Here, f is the ion distribution function, Z is the ion charge, and m is the ion mass. In collisionless simulation, $C=0$. $\mathbf{B}_0\equiv B_0\mathbf{b}_0$ is the equilibrium magnetic field. In electrostatic simulation $\mathbf{B}\equiv\mathbf{B}_0$, and $\mathbf{B}^*$ is defined as

$$\mathbf{B}^*=\mathbf{B}_0^*=\mathbf{B}_0+\frac{B_0v_\parallel}{\Omega}\nabla\times\mathbf{b}_0. \tag{4}$$

Here, $\Omega=ZB_0/cm$ is the gyrofrequency. The $\mathbf{E}\times\mathbf{B}$ drift velocity $\mathbf{v}_E$ is defined as

$$\mathbf{v}_E=\frac{c\mathbf{b}_0\times\nabla\langle\phi\rangle}{B_\parallel^*}. \tag{5}$$

Here, ϕ is the electrostatic potential and $\langle\ldots\rangle$ is the gyro-averaging. $\langle a\rangle=\frac{1}{2\pi}\oint d\zeta\int d\mathbf{x}a(\mathbf{x})\delta(\mathbf{x}-\mathbf{X}-\boldsymbol{\rho})$ with ζ being the gyro-phase angle and $\boldsymbol{\rho}=cm\mathbf{b}_0\times\mathbf{v}/(ZB_0)$ being the gyro-radius. $B_\parallel^*=\mathbf{B}^*\cdot\mathbf{b}_0$. The magnetic gradient drift velocity is expressed as

$$\mathbf{v}_g=\frac{c\mu}{Z_\alpha B_\parallel^*}\mathbf{b}_0\times\nabla B_0. \tag{6}$$

In the limit of $k_\perp L_p\gg1$, where L_p is the characteristic length of the pressure profile, the gyrokinetic Poisson equation can be written as

$$\frac{Z_i^2n_{i0}}{T_{i0}}\left(\phi-\tilde{\phi}\right)=Z_i\langle n_i\rangle-en_e, \tag{7}$$

where $n_\alpha=n_{\alpha0}+\delta n_\alpha$ ($\alpha=i,e$) is the total particle density for ions ($\alpha=i$) and electron ($\alpha=e$) with $n_{\alpha0}$ being the equilibrium component and δn_α the perturbed component. T_{i0} and T_{e0} are the equilibrium ion and electron temperatures. ϕ is the fluctuation electrostatic potential and $\tilde{\phi}(\mathbf{x},t)$ is the double averaged potential defined as

$$\tilde{\phi}(\mathbf{x},t)=\int dv\int dX\langle\phi\rangle(\mathbf{X},t)f_0(\mathbf{X},t)\delta(\mathbf{x}-\mathbf{X}-\boldsymbol{\rho}), \tag{8}$$

with the quasi-neutral condition for the equilibrium part and adiabatic-electron assumption. The gyrokinetic Poisson equation can be written as

$$\frac{Z_i^2n_{i0}}{T_{i0}}\left(\phi-\tilde{\phi}\right)=Z_i\langle\delta n_i\rangle-en_{e0}\frac{e\delta\phi}{T_e}. \tag{9}$$

Here, $\delta\phi$ is the non-zonal part of fluctuation potential. Therefore, we can calculate ϕ with $\delta\bar{n}_i$. The way to compute $\langle\delta n_i\rangle$ is different in δf simulation and *full-f* simulation. In the δf, we can calculate the $\langle\delta n_i\rangle$ by

$$\langle\delta n_i\rangle=\int d\mathbf{v}\int d\mathbf{R}\delta f(\mathbf{R})\delta(\mathbf{X}-\mathbf{R}-\boldsymbol{\rho}). \tag{10}$$

The value of δf can be calculated from the weight equation. In the *full-f* simulation, the ion density perturbation is calculated by

$$\langle\delta n_i\rangle=\int d\mathbf{v}\int d\mathbf{R}f(\mathbf{R})\delta(\mathbf{X}-\mathbf{R}-\boldsymbol{\rho})-n_0. \tag{11}$$

In the δf simulation, to reduce the particle noise, we separate the distribution function and the propagator into equilibrium part and perturbed part $f=f_0+\delta f$ and $\mathcal{L}=\mathcal{L}_0+\delta\mathcal{L}$, the equilibrium part satisfies the gyrokinetic equation

$$L_0f_0=0. \tag{12}$$

03 November 2026 18:38:41

© Author(s) 2026

Here,

$$\mathcal{L}_0 = \frac{\partial}{\partial t} + \left(v_\parallel \mathbf{b}_0 + \mathbf{v}_g\right)\cdot\nabla - \frac{\mu}{m}\mathbf{B}^*\cdot\frac{\nabla B}{B_\parallel^*}\frac{\partial}{\partial v_\parallel} \tag{13}$$

and

$$\delta\mathcal{L} = \mathbf{v}_E\cdot\nabla - \frac{Z_i}{m}\mathbf{B}^*\cdot\frac{\nabla\phi}{B_\parallel^*}\frac{\partial}{\partial v_\parallel}. \tag{14}$$

The perturbed part satisfies

$$\mathcal{L}\delta f = -(\delta\mathcal{L})f_0. \tag{15}$$

We can then define marker weight $w = \delta f/f$, then the gyrokinetic Valsov equation can be expressed as

$$\frac{dw}{dt} = (1-w)\left[-\mathbf{v}_E\cdot\frac{\nabla f_0}{f_0} + \frac{Z_i}{mf_0}\frac{\mathbf{B}^*}{B_\parallel^*}\cdot\nabla\phi\frac{\partial f_0}{\partial v_\parallel}\right]. \tag{16}$$

If we take f_0 to be LM, which is a good approximation of the steady-state solution of gyrokinetic Vlasov equation when the particle drift orbit width is small compared with the scale length of the pressure gradients, we have

$$f_0 = N_{LM}(\psi)\left(\frac{m}{2\pi T_{LM}(\psi)}\right)^{\frac{3}{2}}\exp\left(-\frac{\frac{1}{2}mv_\parallel^2 + \mu B(\psi,\theta)}{T_{LM}(\psi)}\right). \tag{17}$$

The weight equation based on the local Maxwellian is expressed as

$$\frac{dw}{dt} = (1-w)\left[\mathbf{v}_E\cdot\boldsymbol{\kappa} - \frac{Z_i}{T_{LM}}v_\parallel\frac{\mathbf{B}^*}{B_\parallel^*}\cdot\nabla\phi\right]. \tag{18}$$

Here, $\boldsymbol{\kappa}$ is defined as

$$\kappa = \frac{\nabla N_{LM}(\psi)}{N_{LM}} + \left(\frac{\mu B_0}{T_{LM}} + \frac{mv_\parallel^2}{2T_{LM}} - \frac{3}{2}\right)\frac{\nabla T_{LM}}{T_{LM}}. \tag{19}$$

B. Canonical loading method

The exact solution of the collisionless gyrokinetic equation in the axisymmetric toroidal configuration is given by three constants of motion (CoM),[9] which are canonical toroidal angular momentum P_ζ, magnetic momentum μ, and particle energy E, defined as

$$\begin{aligned} P_\zeta &= -\frac{Z}{c}\psi + \frac{RB_\zeta}{B}\frac{m}{Z}v_\parallel,\\ \mu &= \frac{\frac{1}{2}mv_\perp^2}{B},\\ E &= \frac{1}{2}m\left(v_\perp^2 + v_\parallel^2\right). \end{aligned} \tag{20}$$

Here, Z is the particle charge, c is the speed of light, ψ is the poloidal flux function, B_ζ is the toroidal component of the magnetic field $\mathbf{B}$, R is the major radius, m is the mass of the particle, $v_\parallel$ is the parallel velocity, and $v_\perp$ is the perpendicular velocity. In Boozer coordinates, the covariant representation of magnetic field is

$$B = \delta(\psi,\theta,\zeta)\nabla\psi + I(\psi)\nabla\theta + g(\psi)\nabla\zeta, \tag{21}$$

and the contravariant form is $\mathbf{B} = q(\psi)\nabla\psi\times\nabla\theta - \nabla\psi\times\nabla\zeta$.

These three constants of motion can then be expressed in the Boozer coordinate,

$$\begin{aligned} P_\zeta &= -\frac{Z}{c}\psi + \frac{g}{B}\frac{m}{Z}v_\parallel,\\ E &= \frac{1}{2}mv_\parallel^2 + \mu B. \end{aligned} \tag{22}$$

Based on the principle of maximum entropy, the CM distribution function has the Maxwellian-like form

$$F_{COM} = C_{COM}(P_\zeta,\mu,E)\exp\left(-\frac{E}{T_{COM}(P_\zeta,\mu,E)}\right). \tag{23}$$

Due to the coupling of spatial and velocity space in constant motion coordinates, it can be challenging to design the radial temperature and density profiles to match those of a given radial equilibrium profile in experiment. In this section, we will present a method consisting of three modification steps for iteratively adjusting the CM to approximate a specific LM with certain density and temperature profiles and initialize the position and velocity of particles to follow the CM (canonical loading). The LM with a given density profile $N_{LM}(\psi)$ and temperature profile $T_{LM}(\psi)$ can be written as

$$F_{LM} = N_{LM}(\psi)\left(\frac{m}{2\pi T_{LM}(\psi)}\right)^{\frac{3}{2}}\exp\left(-\frac{\frac{1}{2}mv_\parallel^2 + \mu B}{T_{LM}(\psi)}\right). \tag{24}$$

Rewriting Eq. (22) by $v_\parallel = \mathrm{sign}(v_\parallel)\sqrt{2(E-\mu B(\psi,\theta))/m}$, we have

$$\begin{aligned} \frac{Z}{c}\psi &= -P_\zeta + \mathrm{sign}(v_\parallel)\frac{g(\psi)}{B(\psi,\theta)}\frac{m}{Z}\sqrt{\frac{2(E-\mu B(\psi,\theta))}{m}},\\ v_\parallel &= \mathrm{sign}(v_\parallel)\sqrt{\frac{2(E-\mu B(\psi,\theta))}{m}}. \end{aligned} \tag{25}$$

We can now approximate ψ and $v_\parallel$ by iteration,

$$\begin{aligned} \frac{Z}{c}\psi_{COM}^{(n)} &= -P_\zeta + \frac{g\left(\psi_{COM}^{(n-1)}\right)}{B\left(\psi_{COM}^{(n-1)},\theta_c\right)}\frac{m}{Z}v_{\parallel\,COM}^{(n)},\\ v_{\parallel\,COM}^{(n)} &= (-1)^i\sqrt{\frac{2\left(E-\mu B\left(\psi_{COM}^{(n-1)},\theta_c\right)\right)}{m}}. \end{aligned} \tag{26}$$

Here, n denotes the iteration number, and ψ_{COM}^n and $v_{\parallel,COM}*(n)$ represent the canonical magnetic flux and canonical parallel velocity, respectively, after n iterations. The subscript i labels the particle. The iteration is initialized by setting $\psi_{COM}^0 = -P_\zeta$, with ψ_{COM} constrained to the interval $[\psi_0, \psi_1]$. When $E < \mu B\left(\psi_{COM}^{n-1}, \theta_c\right)$, $v_{\parallel,COM}^n$ is set to zero. Here, θ_c is a prescribed constant and is set to π in the following simulations. We have also examined $\theta_c = 0$ and $\theta_c = \pi/2$ and found only negligible differences compared with the results obtained using $\theta_c = \pi$. This iterative procedure, which yields the CM after n iterations, is hereafter referred to as the first modification step,

$$F_{CM} = N_{LM}\left(\psi_{COM}^{(n)}\right)\left(\frac{m}{2\pi T_{LM}\left(\psi_{COM}^{(n)}\right)}\right)^{\frac{3}{2}}\exp\left(-\frac{E}{T_{LM}\left(\psi_{COM}^{(n)}\right)}\right). \tag{27}$$

03 November 2026 18:38:41

© Author(s) 2026

After the form of the CM is decided, the marker particle is loaded according to the LM, while the marker particle with the particle weight $p = F_{CM}/F_{LM}$. The particle distribution thus follows the F_{CM} since

$$\int 1 \times F_{CM}\, Jd\mathbf{V} = \int \frac{F_{CM}}{F_{LM}} F_{LM}\, Jd\mathbf{V} = \int pF_{LM} Jd\mathbf{V}.$$

We perform a convergence test of iteration time to find the best iteration time. The equilibrium density profile $N_{LM}(\psi)$ and temperature profile $T_{LM}(\psi)$ in this convergence test are taken from Ref. 2. A cyclone like[25] density profile and temperature profile are used in the loading and can be expressed as follows:

$$\begin{aligned} N_{LM}(\psi) &= N_0 \exp\left(-a \tanh \frac{\psi/\psi_W - \psi_0}{b}\right), \\ T_{LM}(\psi) &= T_0 \exp\left(-c \tanh \frac{\psi/\psi_W - \psi_0}{d}\right). \end{aligned} \tag{28}$$

With $a = 0.215$, $c = 0.415$, and $b = d = 0.40$, $N_0 = 1.13 \times 10^{13}\ \mathrm{cm}^{-3}$ is the on-axis ion density and $T_0 = 5.00\ \mathrm{keV}$ is the on-axis ion temperature. The major radius $R_0 = 83.5\ \mathrm{cm}$ and minor radius $a = 29.8\ \mathrm{cm}$ with $a/\rho_i = 83.3$. $\rho_i = C_s/\Omega$ is the gyroradius. The toroidal magnetic field on the magnetic axis $B_0 = 2.0125\ \mathrm{T}$. At minor radius $r = 0.5$, $R_0/L_T = 6.9$, $L_n/L_T = 3.2$, safe factor $q = 1.4$, $(r/q)/(dq/dr) = 0.78$. ψ_W is the poloidal magnetic flux at the last closed magnetic flux surface. $L_T = -(d \ln T/dr)^{-1}$ and $L_n = -(d \ln n/dr)^{-1}$ are the characteristic lengths of temperature profile and density profile. The radial profile of the CM after the fourth iteration in the first modification step closely matches that of the LM, showing only a 10% difference after the fourth iteration and further iterations yield no significant improvement, as shown in Fig. 1, so we adopt four iterations subsequently.

However, for micro-instability simulations, such as ITG, the linear dispersion relation is strongly related to the profile gradient,[25] a more accurate match to the radial profile requires further modification of the CM. If a certain CM has radial density and temperature profile as

$$\begin{aligned} N_{load}(\psi) &= \int F_{CM}(P_\zeta, \mu, E) Jd\theta d\zeta d\Theta dv_\parallel d\mu, \\ T_{load}(\psi) &= \int EF_{CM}(P_\zeta, \mu, E) Jd\theta d\zeta d\Theta v_\parallel d\mu. \end{aligned} \tag{29}$$

Here, $J = \frac{B_\parallel^*}{m} \cdot \frac{gq+I}{B_0^2}$ is the gyrocenter phase-space Jacobian. We define the modification factors $w_{nload}(\psi_{CM})$ and $w_{tload}(\psi_{CM})$ written as

$$\begin{aligned} w_{nload}(\psi_{CM}) &= \frac{\langle N_{load}(\psi_{CM})\rangle}{N_{LM}(\psi_{CM})}, \\ w_{tload}(\psi_{CM}) &= \frac{\langle T_{load}(\psi_{CM})\rangle}{T_{LM}(\psi_{CM})}. \end{aligned} \tag{30}$$

For a given tokamak geometry, the integral cannot be calculated analytically. The density and temperature profiles are obtained by particle loading. Here, $\langle \ldots \rangle$ means smooth on ψ_{CM}. The new CM becomes

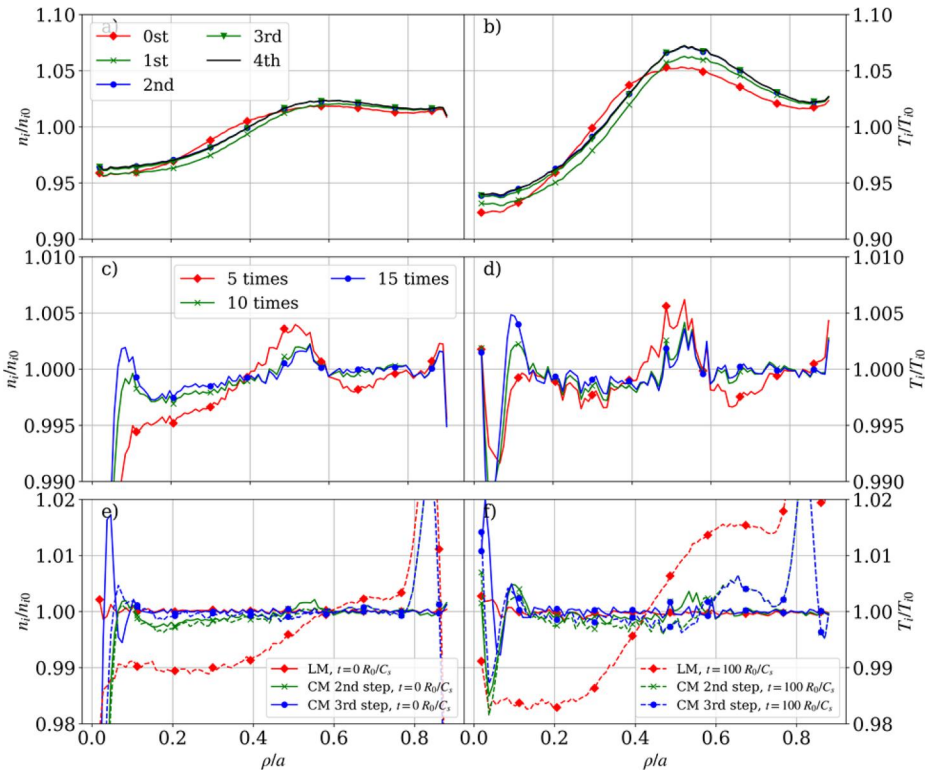


FIG. 1. The radial density and temperature profile by canonical loading normalized to the target density and temperature radial profile after the first modification step [panel (a) and panel (b)] and second modification step [panel (c) and panel (d)]. The density and temperature profiles change in $100R_0/C_s$ with LM and CM after the 2nd modification step and the third modification step [panel (e) and (f)]. The density and temperature profile from loading is divided by the target profile.

03 November 2026 18:38:41

© Author(s) 2026

$$F_{CM} = N'_{CM}(P_\zeta, \mu, E)\left(\frac{m}{2\pi T'_{CM}(P_\zeta, \mu, E)}\right)^{\frac{3}{2}} \times \exp\left(-\frac{E}{T'_{CM}(P_\zeta, \mu, E)}\right). \tag{31}$$

Here,

$$N'_{CM}(P_\zeta, \mu, E) = N_{CM}(P_\zeta, \mu, E)/w_{nload}(\psi_{CM}),$$
$$T'_{CM}(P_\zeta, \mu, E) = T_{CM}(P_\zeta, \mu, E)/w_{tload}(\psi_{CM}). \tag{32}$$

We iteratively apply this method as the second modification step to construct a CM that closely matches the density and temperature profiles of a given LM. The results indicate that after 15 iterations in the second modification step, the radial profile of the CM deviates from the equilibrium profile by less than 0.1%, as shown in Fig. 1. Based on this convergence threshold, we adopted 15 iterations to generate the CM in our simulations.

To get the particle distribution with an exact radial equilibrium profile, we use a similar modification method as the third modification step by defining a new modification factor,

$$w_{nload}(\psi) = \frac{N_{load}(\psi)}{N_{LM}(\psi)}, \quad w_{tload}(\psi) = \frac{T_{load}(\psi)}{T_{LM}(\psi)}, \tag{33}$$

and the new CM becomes

$$F_{CM} = N'_{CM}(P_\zeta, \mu, E)\left(\frac{m}{2\pi T'_{CM}(P_\zeta, \mu, E)}\right)^{\frac{3}{2}} \times \exp\left(-\frac{E}{T'_{CM}(P_\zeta, \mu, E)}\right), \tag{34}$$

where

$$N'_{CM}(P_\zeta, \mu, E) = N_{CM}(P_\zeta, \mu, E)/w_{nload}(\psi),$$
$$T'_{CM}(P_\zeta, \mu, E) = T_{CM}(P_\zeta, \mu, E)/w_{tload}(\psi). \tag{35}$$

However, it should be noted that this modification method does not preserve the exact form of the CM. We emphasize that the third modification step is introduced solely to provide an exact initial condition that matches the prescribed radial profile, and this step is not required in the production simulations. To better assess the impact of this non-canonical adjustment, we performed a Monte Carlo simulation to analyze the resulting profile variations. The results show that after the third modification step, the density profile variation is around 0.1%. CM is comparable to the initial deviation from the equilibrium profile as shown in Fig. 1. In contrast, the temperature profile variation is larger, approximately 1%. Notably, the radial profile variation in simulations using the CM is much smaller than that observed with the LM.

III. VERIFICATION OF FULL-F SIMULATION

A. Linear verification

To verify electrostatic *full-f* simulations, the marker particles are initialized according to LM and CM, respectively, with the same density and temperature radial profile as in the canonical loading. In both simulations, we use $N_r = 96$, $N_\theta = 394$, and $N_\parallel = 16$ for radial, poloidal, and parallel grid numbers and different marker particle numbers for convergence tests. A Gaussian boundary decay is applied from $r/a = 0.094$ to 0.14 and $r/a = 0.76$ to 0.89. To reduce the initial fluctuation amplitude arising from discrepancies between the loaded particle distribution and the equilibrium distribution—particularly near the radial boundaries and due to the final modification in the canonical loading—a preconditioning Monte Carlo procedure is performed for several bounce periods until the system attains a steady state without self-consistent electrostatic potentials. The time-averaged particle density profile from this steady state is then used as the new equilibrium profile, serving as the initial condition for the subsequent nonlinear simulations.

The CM distribution is closer to the exact equilibrium distribution than the LM. Consequently, simulations initialized with the CM require a shorter preconditioning time for the Monte Carlo procedure to reach a steady state. In the CM case, the Monte Carlo preconditioning simulation is performed from $t = 0$ to $28R_0/C_s$, with the system reaching steady state at approximately $t = 10R_0/C_s$. The time-averaged particle density profile over the interval $t = 20$–$28R_0/C_s$ is then adopted as the equilibrium density profile for the subsequent self-consistent turbulence simulation, which begins after $t = 28R_0/C_s$. In contrast, for the LM initialization, the Monte Carlo simulation is carried out from $t = 0$ to $68R_0/C_s$, with the system attaining steady state around $t = 50R_0/C_s$. The time-averaged density profile between $t = 60$ and $68R_0/C_s$ is employed as the equilibrium profile, and the self-consistent turbulence simulation starts thereafter. Each simulation uses 3000 marker particles per cell to ensure convergence. The resulting ITG linear growth rates show that the *full-f* simulation initialized with the CM yields $\gamma_{CM} = 0.107C_s/R_0$, which is in excellent agreement with the δf simulation result based on LM $\gamma_{\delta f} = 0.105C_s/R_0$. The mode structure (Fig. 2) in the linear stage and mode saturation amplitude at the early saturation stage ($t = 44R_0/C_s$) also show agreement with δf simulation. In contrast,

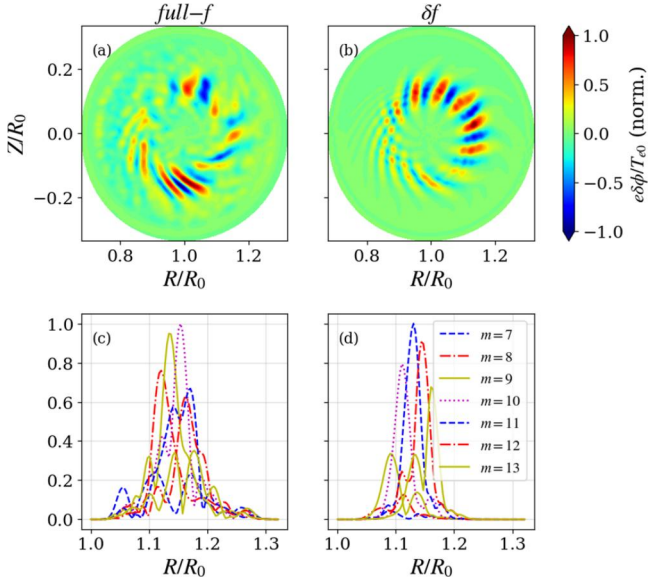


FIG. 2. The fluctuation potential at constant Boozer toroidal angle $\zeta = 0$ in *full-f* [panel (a) at $t = 36R_0/C_s$] and δf [panel (b) at $t = \frac{20R_0}{C_s}$] simulations and the radial profile of the absolute amplitude of each poloidal Fourier harmonics in *full-f* [panel (c)] and δf [panel (d)]. The fluctuation level has been renormalized by its maximum value.

03 November 2026 18:38:41

© Author(s) 2026

the LM-based *full-f* simulation gives a lower growth rate of $\gamma_{\mathrm{LM}} = 0.093 C_s/R_0$. The difference in growth rates originates from the distinct equilibrium profile gradients established during the preconditioning simulation. In the LM case, the temperature profile undergoes substantial flattening as the system relaxes toward equilibrium, with the radially averaged R_0/L_T averaged over $r/a = 0.3 - 0.5$ decreasing from its initial value of 6.25 to 5.94. In contrast, the equilibrium profile in the CM case remains nearly unchanged, with $R_0/L_T = 6.24$. Because the linear growth rate of the ion temperature gradient (ITG) mode is highly sensitive to the background temperature gradient,[25] these post-preconditioning profile differences naturally account for the observed variation in linear growth rates.

B. Nonlinear verification

Figure 3 shows the convergence for marker particle numbers in the full-f simulations. The convergence test for the number of marker particles indicates that 1000 particles per cell are sufficient for the ITG turbulence simulation. In the nonlinear stage of *full-f* simulation, we can see that the amplitude of modes tends to decrease over time due to the relaxation of the plasma temperature profile because of the ion heat transport. However, it is desirable to sustain the steady state of turbulence with constant temperature gradient drive. One way to achieve this is to prevent temperature profile from relaxing by introducing proper heat bath. In this section, we carry out simulation with heat bath to maintain the temperature gradient. If we take equilibrium temperature profile to be $T_0(r)$. At certain time in the nonlinear stage the temperature profile relaxes to $T_1(r)$. Then, the energy of one particle located at r is changed by the heat bath as Eq. (36) to keep the pitch angle $\lambda = \mu/E$ as an invariant. A similar heat bath is also applied in the δf simulation. Notably, the heating model used here differs from the usual constant-power source–sink CM commonly adopted in *full-f* flux-driven simulations.[18,26–28] Experimentally, substantial profile evolution typically occurs on the order of 100 ms,[29,30] whereas over O(1 ms), the profiles are essentially stationary. Because the present simulations span ∼1 ms, we impose a heat-bath condition that fixes the temperature profile for simplicity, thereby preventing spurious profile changes associated with artificial sources and sinks. In future work, we plan to implement a more realistic heating scheme that is intended to mimic the experimental conditions, but this is not considered in the present study,

$$v_\parallel = v_{\parallel 0}\sqrt{\langle T_0(r)\rangle/\langle T_1(r)\rangle}, \qquad \mu = \mu_0\langle T_0(r)\rangle/\langle T_1(r)\rangle. \tag{36}$$

Here, $\langle \ldots \rangle$ means radial smoothing and time averaging in $2R_0/C_s$. The heat bath can be described as a source term $S = -E\frac{\partial f}{\partial E}|_\lambda \left(\frac{\langle \int Ef d\mathbf{v}\rangle}{\langle E f_0 d\mathbf{v}\rangle} - 1\right)$.

A fundamental distinction emerges in the steady-state behavior between δf and *full-f* simulations. The *full-f* simulation with a heat bath to fix the temperature profile sustains much higher levels of fluctuation potential and ion heat transport throughout the simulation. Both δf simulations and *full-f* simulations without fixing temperature profiles exhibit significant transport reduction, ultimately approaching zero transport. In the long-time δf simulation, the transport continuously drops as increasingly large marker weights contribute to the formation of a coherent structure and amplify the sampling noise. Moreover, the δf simulation with local Maxwellian implicitly treats it as the equilibrium solution to the collisionless Vlasov equation, which is not strictly valid. Consequently, the late-time mode spectrum becomes dominated by a large $(m, n) = (0, 1)$ component, which further suppresses the turbulence, as also observed in Ref. 9. In the *full-f* simulation without heat bath, the normalized temperature gradient $R0/L_T$ decreases to approximately $R_0/L_T = 4.5$ after $t = 200R0/C_s$, approaching the critical threshold for ITG marginal stability.[25] This reduction in driving gradient substantially reduces the turbulent

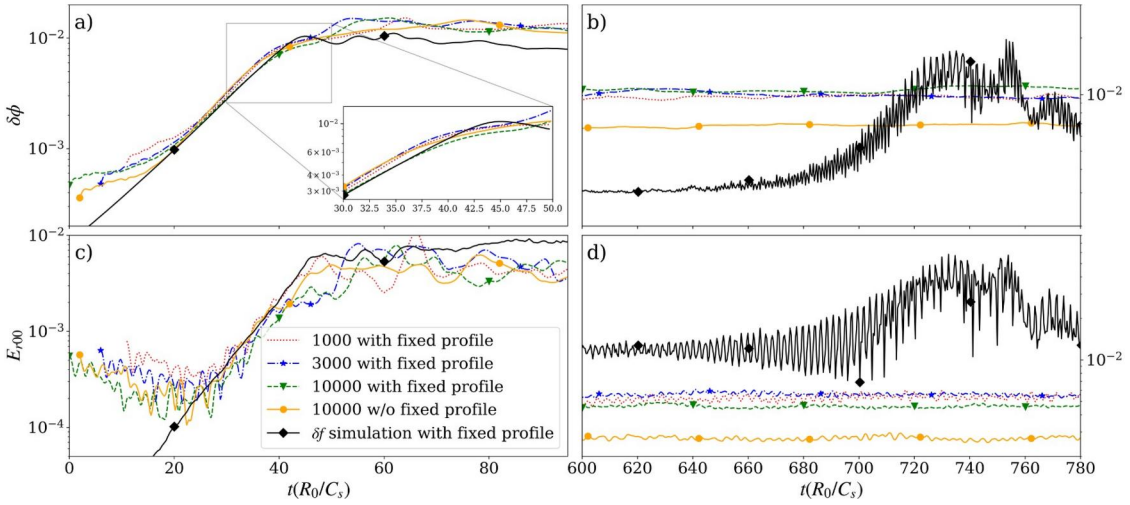


FIG. 3. The time history of non-zonal electrostatic potential in the early linear and nonlinear stage [panel (a)] and late steady state [panel (b)], zonal electric field in the early linear and nonlinear stage [panel (c)] and nonlinear stage [panel (d)] in *full-f* simulations with and w/o fixed temperature profile by a heat bath. The δf simulation result (black line) is shown for comparison. All quantities shown here are root mean square, non-zonal averaged from $r \in [0.45a - 0.5L_T, 0.45a + 0.5L_T]$, and over all poloidal and toroidal angles, where the linear mode peaks at $r = 0.45a$.

03 November 2026 18:38:41

© Author(s) 2026

transport. In contrast, the *full-f* simulation with heat bath preserves the temperature profile gradient throughout the simulation, sustaining continuous drift wave turbulence and yielding steady-state heat transport levels of approximately $0.035\chi_{GB}$. At $t = 640R0/C_s$, the δf simulation exhibits rapid growth in fluctuation potential with large zonal flow oscillations. This is typically manifested in δf simulations due to accumulated particle noise from large particle weight, which will not appear in *full-f* simulations.

IV. LONG-TIME NONLINEAR DYNAMICS OF ITG TURBULENCE

In the long-time *full-f* turbulence simulation using CM, a distinct transition phenomenon can be observed around $t \approx 250R_0/C_s$, marking a significant change in both turbulent transport characteristics and zonal flow dynamics. This transition separates two distinct regimes, each with notably different physical behaviors, as illustrated in Fig. 4

Before the transition, the turbulence propagates radially inward at a velocity of $v_{\text{turb}} = 0.005\,67C_s$ at $r/a > 0.4$, which is close to the diamagnetic velocity $v_* = \rho_i C_s/L_n = 0.005\,60C_s$ at $r = 0.4a$. Such turbulence behavior has been recognized as a turbulence avalanche.[18,31,32] Multiple bursts of turbulence intensity can also be observed, with the peak of the burst decaying with simulation time. Concurrently, radially inward-propagating structures are also observed in the zonal flow shear, with a time frequency $\omega = 0.188C_s/R_0$, approximately $0.1\omega_{\text{GAM}}$, and a radially inward propagation velocity $v_{zf} = 0.000\,571C_s$, which is approximately $v_{\text{turb}}/10$. The zonal flow propagation ends at core, where a strong zero-frequency mean flow builds up at around $r/a \in [0.20, 0.33]$. The outer bound of the mean-flow region gradually extends to $r/a = 0.4$ at $t = 350R_0/C_s$.

Following the transition, the zonal flow shear behaviors reveal three distinct radial regions, each exhibiting unique characteristics.

Region 1: In the outer region $(r/a \in [0.50, 0.77])$, clear radially inward-propagating structures are observed, with a gradual slowing down of the propagation velocity and frequency until $t = 600R_0/C_s$ the zonal flow spectrum is dominated by the zero-frequency component.

Region 2: In the middle region $(r/a \in [0.33, 0.50])$, the zero-frequency zonal flow is dominant, with radially inward-propagating structures persisting, but with a much faster propagation velocity of $v_{zf} = 0.003\,03C_s \approx v_{\text{turb}}/1.87$.

Region 3: In the inner region $(r/a \in [0.14, 0.33])$, the zonal flow shows no propagation with near-zero frequency and velocity. This region is characterized by a long decorrelation time and length, indicating highly persistent, coherent zonal flow structures in the core.

Because the simulations employ an adiabatic-electron model, the electron density profile remains unchanged. Moreover, in simulations with the heat bath, the temperature profile is maintained and prevented from flattening. Because the transition persists under these conditions, it cannot be attributed to the temperature profile flattening observed in simulations without the heat bath. Instead, the transition is primarily associated with the self-consistent evolution of the particle phase-space distribution, zonal flows, and turbulence. Following the transition, the system gradually approaches a nonlinear steady state in which the distribution function becomes self-consistent with the coupled zonal flow–turbulence dynamics. Here, we primarily focus on the dynamics of the zonal flow. To quantify the zonal flow suppression of the turbulence, we compute the effective shearing rate,[16] which suppresses turbulence when it exceeds the ambient turbulence decorrelation rate (approximated by the ITG linear growth rate). The effective shearing rate is defined as[16]

$$\omega_{eff} = \omega_E \frac{\left[\left((1+3F)^2 + 4F^3\right)^{\frac{1}{4}}\right]}{\left[(1+F)\sqrt{1+4F}\right]}, \tag{37}$$

where $\omega_E = -\partial^2\Phi_{00}(\psi)/\partial\psi^2 \cdot (\Delta\psi_0/\Delta\phi)$ is the zonal flow shearing rate and $F \equiv \omega_f^2/\Delta\omega_T^2$. Here, Φ_{00} is the zonal part of the fluctuation potential. $\Delta\psi_0\, R\, B_\theta$ is the radial correlation length and $R\Delta\phi$ is the toroidal correlation length. The zonal flow frequency is ω_f, while $\Delta\omega_T$ is the turbulence decorrelation rate, approximated by the ITG linear growth rate. We assume isotropic eddies so that the radial and poloidal correlation lengths are equal. To analyze zonal flow frequency characteristics across the transition, we select three radial–time windows from the zonal flow radial profile. For each window, we compute the two-point correlation function,[33,34] $C_{tr}(\Delta t, \Delta r) = \frac{\langle\phi(t+\Delta t, r+\Delta r)\phi(t,r)\rangle}{\sqrt{(\langle\phi 2(t+\Delta t, r+\Delta r)\rangle\,\langle\phi 2(t,r)\rangle)}}$ to quantify zonal flow properties and their evolution. Here, the $\langle\ldots\rangle$ means average in each time and radial window, as shown in Fig. 5. The turbulence decorrelation time is estimated as the inverse ITG growth rate. The time evolution of the effective shearing rate derived from the correlation analysis in the three regions is shown in Fig. 5.

From Figs. 4(b), 5(b), and 5(e), a gradual slowing of inward zonal flow propagation is evident in Region 1. The decay of the propagation velocity lowers the zonal flow frequency, which in turn increases the effective shearing rate and further suppresses the turbulence. In Regions 2 and 3, a sudden transition is observed, as shown in Figs. 5(e) and 5(h). After the transition, zonal flow propagation abruptly disappears, and zero-frequency zonal flows dominate. This transition is likewise reflected in the transport, where the turbulence settles into a quasi-steady state with a much lower transport level

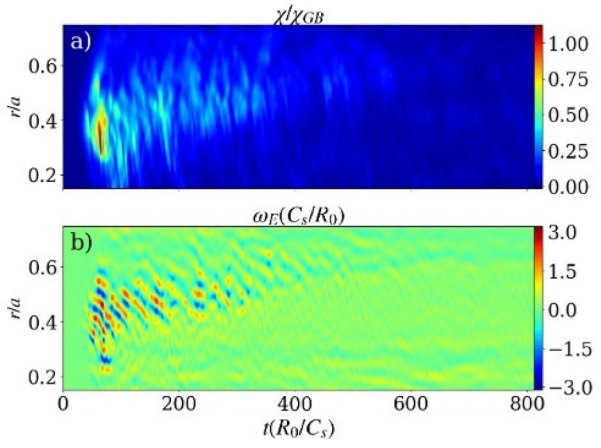


FIG. 4. Time history of radial profile of ion heat conductivity $\chi_i \equiv \langle \int v_{dr}(E - 1.5T) f d\mathbf{v} \rangle L_T/nT$ [panel (a)] normalized to gyro-Bohm unit and zonal flow shearing rate ω_E (panel b). Here, $\langle\rangle$ means average over the flux surface and $\int d\mathbf{v}$ is the velocity space integral. T is the local temperature, v_{dr} is the radial $E \times B$ drift from perturbed electric fields. $\chi_{GB} = \rho_i^2 C_s/L_T$ is the gyro-Bohm unit.

03 November 2026 18:38:41

© Author(s) 2026

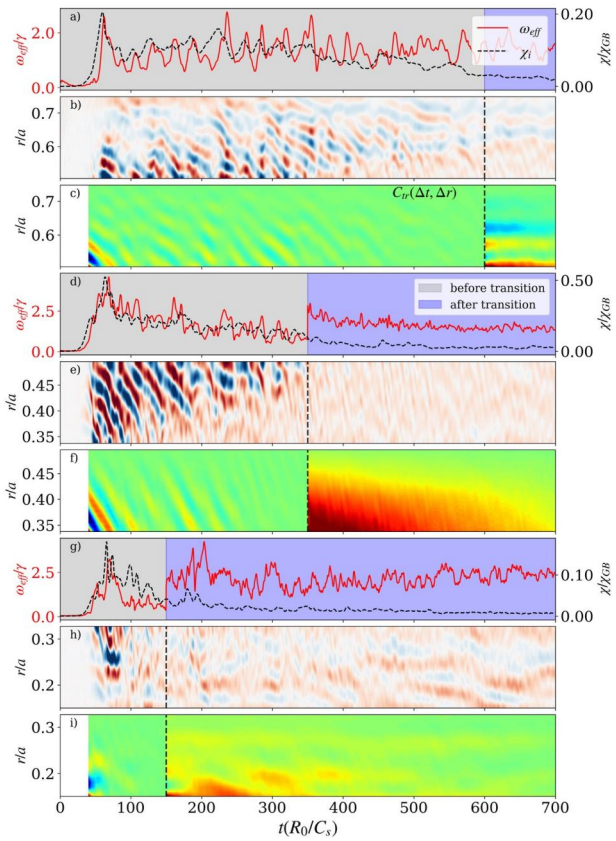


FIG. 5. Time evolution of turbulent transport, the effective zonal flow shearing rate, and the corresponding spatiotemporal structure and autocorrelation of the zonal flow shear. The figure is divided into three radial regions, displayed from the outer region at the top to the inner region at the bottom. Panels (a), (d), and (g) show the volume-averaged effective shearing rate ω_{eff}/γ (red solid curves) and ion heat conductivity χ_i/χ_{GB} (black dashed curves). Panels (b), (e), and (h) show the corresponding time-radius evolution of the normalized zonal flow shearing rate ω_E/γ. Panels (c), (f), and (i) show its normalized spatiotemporal autocorrelation $C_{tr}(\Delta t, \Delta r)$. Panels (a)–(c), (d)–(f), and (g)–(i) correspond to the radial ranges $0.50 < r/a < 0.76$, $0.33 \lesssim r/a \lesssim 0.50$, and $0.14 \lesssim r/a \lesssim 0.33$, respectively. The vertical dashed lines indicate the transition times $t = 600, 350$, and $150 R_0/C_s$ for the three radial regions. The transition time is determined from the zonal flow dynamics, specifically when the clear radial propagation of the zonal flow ceases. The dominant zonal flow frequency within each window is then calculated using a Fourier transform.

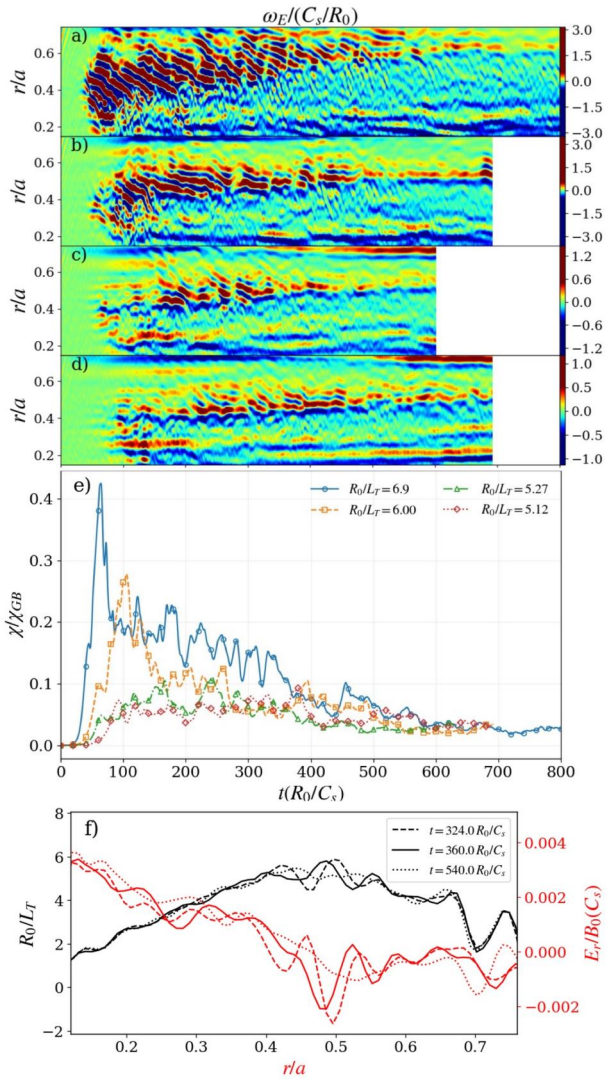


FIG. 6. The time history of the radial profile of zonal flow shearing rate in simulation with different temperature gradients [panel (a) $R_0/L_T = 6.91$, panel (b) $R_0/L_T = 6.00$, panel (c) $R_0/L_T = 5.27$, and panel (d) $R_0/L_T = 5.12$ at $r/a = 0.5$]. The panel (e) is the volume averaged ion heat conductivity in each case. The panel (f) is the comparison of the radial electric field and temperature profile gradient from the simulation with $R_0/L_T = 5.27$.

compared with that before the transition. These zero-frequency zonal flows form long-lived stair-like structures in zonal flows and temperature profile corrugations, which are usually recognized as the **E × B** staircases.[17,35]

The behavior of the **E × B** staircases was also studied in simulations using different temperature gradients, revealing significant variation in zonal flow dynamics across simulations (Fig. 6). Two distinct types of zonal flows were observed: unstable staircase**s**, which propagate and vanish near the core during the early nonlinear stages of strong turbulence, and stable staircases, which exhibit no radial propagation and persist over time in weak turbulence after the transition. This observation is consistent with previous findings[17,36] that the **E × B** staircase is a near-marginal pattern and disappears in the presence of strong turbulence.

In the stronger turbulence cases ($R0/L_T = 6.91$ and 6.00), unstable staircases with finite propagation velocity appear. In contrast, the weaker turbulence ($R0/L_T = 5.27$ and 5.12) develops stable staircases. As the turbulence evolves, the stronger turbulence cases exhibit a pronounced reduction in transport. Meanwhile, the propagation speed of the staircases decreases continuously and eventually approaches zero. The number of staircases also decreases until the system reaches a steady-state transport level of $\chi_i \approx 0.035\chi_{Gb}$, at which point stable staircases emerge. Conversely, the weak turbulence cases

03 November 2026 18:38:41

© Author(s) 2026

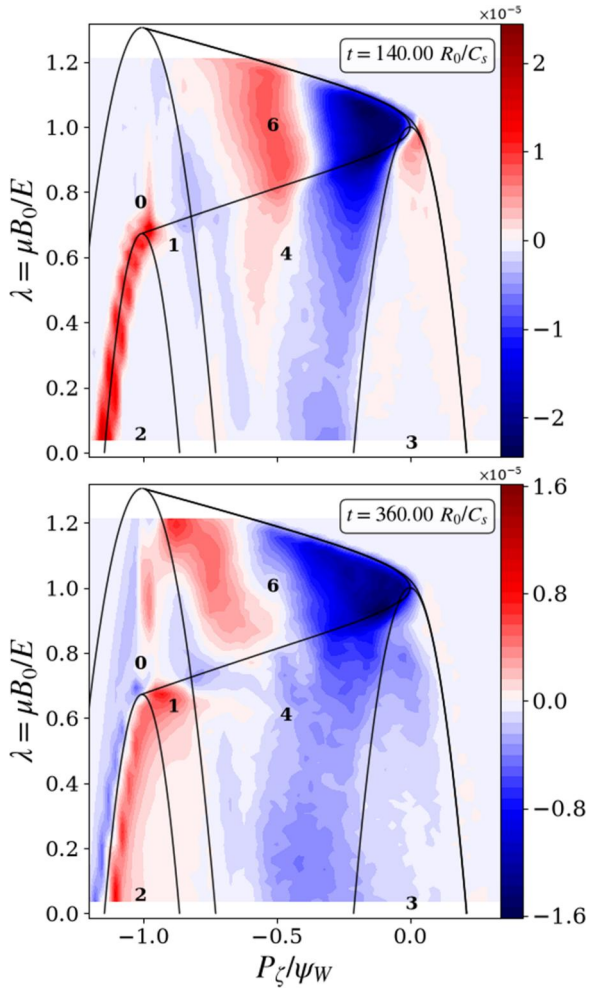


FIG. 7. The phase-space zonal structure of fluctuation density normalized to total particle density in CoM space. The particle distribution is calculated by averaging over particle kinetic energy $1.33T_{e0} < E < 1.56T_{e0}$, where the $\delta f/f_0$ reaches the maximum value. The panel (a) is the particle density at $t = 140R_0/C_s$ subtracted by the particle density at $t = 0R_0/C_s$ while panel (b) is the particle density at $t = 360R_0/C_s$ subtracted by the particle density at $t = 140R_0/C_s$.

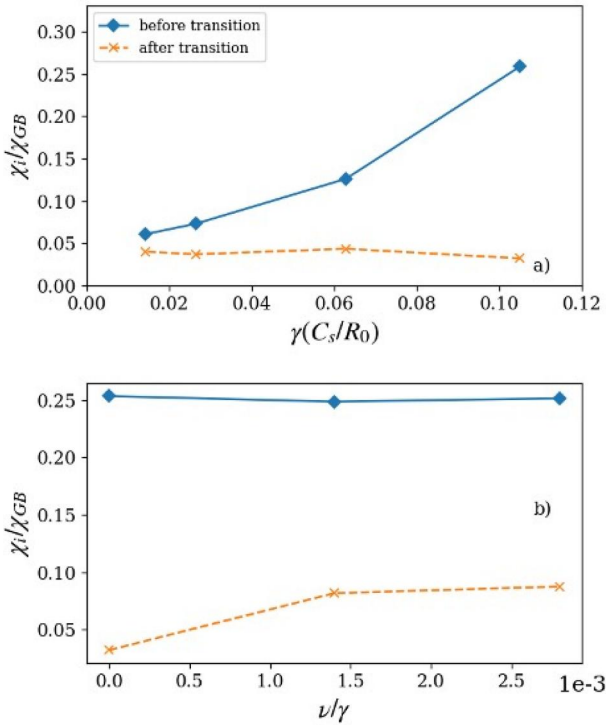


FIG. 8. The volume averaged transport level averaged from $r \in [0.45a - 0.5L_T, 0.45a + 0.5L_T]$ before and after the transition in the simulation with different profile gradients shown in panel (a). The transport level before transition shows weak scaling with collision frequency, while after the transition it shows stronger dependence on the collision frequency, as shown in panel (b). We define the transport level before the transition as χ_L and the transport level after the transition as χ_H. The transition ratio is then defined as the ratio of χ_L to χ_H. It is evident that the transition ratio exhibits an almost linear dependence on the linear growth rate.

[Figs. 6(c) and 6(d)] first exhibit increasing transport until the threshold is reached, at which point unstable staircases appear. After this transition, transport drops below the threshold and remains stable; the weakest case consistently maintains low transport, characterized by persistent stable staircases without a clear transition. In the steady-state turbulence, two stable $\mathbf{E} \times \mathbf{B}$ staircases can be identified at around $r/a = 0.2$, 0.5. In each case, the $\mathbf{E} \times \mathbf{B}$ staircases are accompanied by corrugations in the temperature profile, consistent with the radial force-balance relation, whereby peaks in E_r correspond to minima in the radial temperature gradient,[17,36] as shown in Fig. 6(f). In the steady-state turbulence, the turbulence avalanche starts from the radial position of the staircases and propagates inward and outward. The scan of different collisionalities on $\mathbf{E} \times \mathbf{B}$ staircases also shows that the $\mathbf{E} \times \mathbf{B}$ strength decreases with collisionality. The staircases propagate inward before becoming stationary in the core region. The associated zonal flow subsequently accumulates near the core, forming a strong mean-flow shear layer.

The transition is also evident in the CoM phase space.[37] As shown in Fig. 7, the phase-space structure of the zonal-density fluctuation[38–40] differs qualitatively before and after the transition. A clear redistribution of trapped and counter-passing ions is evident when the two panels are compared. These changes indicate that the transition in turbulence dynamics and transport is accompanied by an evolution of the particle distribution function. Following the transition, the distribution function gradually relaxes toward a nonlinear state that is self-consistent with the coupled zonal flow–turbulence dynamics. Concurrently, the zonal flow pattern evolves from a predominantly turbulence-driven, propagating flow into a slowly varying equilibrium-flow component. The detailed mechanism underlying this phase-space evolution, including the respective roles of phase-space coherent structures and self-consistent zonal flow dynamics, warrants further investigation.

V. TRANSPORT SCALING

We investigate the dependence of post-transition turbulent transport on equilibrium profiles through simulations with varying

03 November 2026 18:38:41

© Author(s) 2026

temperature and density gradients while maintaining constant $\eta_i \equiv L_n/L_T$. At $r = 0.5a$, we set temperature gradients $R0/L_T = 6.90$, 6.00, 5.27, and 5.12, with corresponding density gradients $R0/L_n = 2.2$, 1.9, 1.7, and 1.6. Figure 8 reveals distinct scaling behaviors for ion heat conductivity across the transition: pre-transition transport exhibits Bohm-like scaling (proportional to γ, increasing with L_T/ρ_i), while post-transition transport follows gyro-Bohm scaling (independent of γ and L_T/ρ_i). The transition ratio scales linearly with the linear growth rate, similar to the transition ratio derived from the L–H transition reduced model. In strong turbulence cases, substantial mean-flow shear after transition significantly suppresses turbulence in the $r < 0.5$ region, confining it to outer regions where near-marginal stability emerges. Weak turbulence scenarios maintain near-marginal stability throughout with no distinct transitions. All simulations ultimately converge toward near-marginal states with similar transport levels.

We also examine dependence of turbulent transport on collisionality by artificially changing the ion–ion collision frequency. Ion–ion collisions are modeled with a linearized Fokker–Planck operator.[41] The results show that the pre-transition transport level depends only weakly on the collision frequency, indicating that it is primarily set by the underlying turbulence drive. In contrast, the post-transition transport exhibits a stronger dependence on collisionality: higher collision frequency corresponds to higher transport. This trend is consistent with larger zonal flow damping at higher collisionality, implying that the post-transition transport level is controlled by the collisional damping rate of zonal flows rather than by the primary linear drive.[42,43] Furthermore, the collision can destroy coherent phase-space structures, which modifies the nonlinear equilibrium distribution function and associated turbulent transport.

VI. CONCLUSION

We have verified and applied the GTC *full-f* gyrokinetic scheme based on the CM to investigate global ITG turbulence. A preconditioning Monte Carlo simulation is employed prior to the self-consistent simulation to minimize the initial deviation from the exact solution of the Vlasov equation. Compared with the conventional δf approach, the CM-based *full-f* scheme achieves close agreement in linear growth rates, mode structures, and early nonlinear saturation levels. To avoid profile relaxation in long-time simulation, an effective heat bath is introduced to maintain an approximately fixed temperature profile.

Long-time simulations reveal a clear transition in the coupled turbulence–ZF system. Before the transition, the turbulence exhibits avalanche-like radial propagation, while the ZFs propagate slowly inward at a characteristic velocity approximately one order of magnitude lower than that of the turbulence. Similar turbulence avalanche dynamics and zonal flow propagating structures have been reported in one-dimensional predator–prey models and previous global *full-f*, flux-driven gyrokinetic simulations. After the transition, the turbulent intensity and ion heat transport decrease substantially, while the ZF dynamics become radially dependent. In Region 1 ($r/a \in [0.50, 0.77]$), the inward ZF propagation gradually weakens; in Region 2 ($(r/a \in [0.33, 0.50]$) and Region 3 ($r/a \in [0.14, 0.33]$), the propagation ceases and a zero-frequency ZF component becomes dominant.

The transition can be related to the reduction in the dominant ZF frequency, which increases the effective ZF shearing rate relative to the linear ITG growth rate, consistent with more effective turbulence suppression. This evolution is accompanied by a transition from Bohm-like to gyro-Bohm-like transport scaling and the establishment of a near-marginal state with persistent ($\mathbf{E} \times \mathbf{B}$) staircases. The post-transition transport also exhibits a stronger dependence on collisionality, consistent with the influence of collisional ZF damping.

ACKNOWLEDGMENTS

This work was supported by the U.S. DOE SciDAC and INCITE programs. Simulations used computing resources at ORNL (DOE Contract No. DE-AC05-00OR22725) and NERSC (DOE Contract No. DE-AC02-05CH11231).

AUTHOR DECLARATIONS

Conflict of Interest

The authors have no conflicts to disclose.

Author Contributions

Haotian Chen: Conceptualization (equal); Data curation (lead); Formal analysis (lead); Investigation (lead); Methodology (lead); Project administration (equal); Software (lead); Validation (lead); Visualization (lead); Writing – original draft (lead); Writing – review & editing (equal). **Pengfei Liu:** Conceptualization (supporting); Data curation (supporting); Funding acquisition (equal); Methodology (supporting); Project administration (supporting); Software (supporting); Supervision (equal); Visualization (supporting); Writing – review & editing (supporting). **Xishuo Wei:** Funding acquisition (equal); Software (supporting); Supervision (equal); Writing – review & editing (supporting). **Zhihong Lin:** Conceptualization (equal); Funding acquisition (lead); Resources (lead); Software (supporting); Supervision (equal); Writing – review & editing (equal).

DATA AVAILABILITY

The data that support the findings of this study are openly available in Zenodo (ITG paper data) at https://zenodo.org/records/23447453, Ref. 44. Raw data were generated at the Perlmutter supercomputer, NERSC (DOE). Derived data supporting the findings of this study are available from the corresponding author upon reasonable request.

REFERENCES

[1]W. W. Lee, "Gyrokinetic particle simulation model," J. Comput. Phys. **72**(1), 243–269 (1987).
[2]Z. Lin, T. S. Hahm, W. W. Lee, W. M. Tang, and R. B. White, "Turbulent transport reduction by zonal flows: Massively parallel simulations," Science **281**(5384), 1835–1837 (1998).
[3]W. Horton, "Drift waves and transport," Rev. Mod. Phys. **71**(3), 735–778 (1999).
[4]Y. Idomura, M. Ida, T. Kano, N. Aiba, and S. Tokuda, "Conservative global gyrokinetic toroidal full-*f* five-dimensional Vlasov simulation," Comput. Phys. Commun. **179**(6), 391–403 (2008).
[5]P. Donnel, X. Garbet, Y. Sarazin, V. Grandgirard, Y. Asahi, N. Bouzat, E. Caschera, G. Dif-Pradalier, C. Ehrlacher, P. Ghendrih *et al.*, "A multi-species collisional operator for full-F global gyrokinetics codes: Numerical aspects and verification with the GYSELA code," Comput. Phys. Commun. **234**, 1–13 (2019).

03 November 2026 18:38:41

© Author(s) 2026

[6]S. Ku, C. S. Chang, R. Hager, R. M. Churchill, G. R. Tynan, I. Cziegler, M. Greenwald, J. Hughes, S. E. Parker, M. F. Adams *et al.*, "A fast low-to-high confinement mode bifurcation dynamics in the boundary-plasma gyrokinetic code XGC1," Phys. Plasmas **25**(5), 056107 (2018).
[7]D. Michels, P. Ulbl, W. Zholobenko, T. Body, A. Stegmeir, T. Eich, M. Griener, G. D. Conway, F. Jenko, and ASDEX Upgrade Team, "Full-*f* electromagnetic gyrokinetic turbulence simulations of the edge and scrape-off layer of ASDEX Upgrade with GENE-X," Phys. Plasmas **29**(3), 032307 (2022).
[8]Z. Lu, G. Meng, R. Hatzky, M. Hoelzl, and P. Lauber, "Full *f* and δf gyrokinetic particle simulations of Alfvén waves and energetic particle physics," Plasma Phys. Controlled Fusion **65**(3), 034004 (2023).
[9]Y. Idomura, S. Tokuda, and Y. Kishimoto, "Global gyrokinetic simulation of ion temperature gradient driven turbulence in plasmas using a canonical Maxwellian distribution," Nucl. Fusion **43**(4), 234–243 (2003).
[10]V. Grandgirard, Y. Sarazin, X. Garbet, G. Dif-Pradalier, P. Ghendrih, N. Crouseilles, G. Latu, E. Sonnendrücker, N. Besse, and P. Bertrand, "Computing ITG turbulence with a full-*f* semi-Lagrangian code," Commun. Nonlinear Sci. Numer. Simul. **13**(1), 81–87 (2008).
[11]T. Vernay, S. Brunner, L. Villard, B. F. McMillan, O. Sauter, S. Jolliet, T. M. Tran, and A. Bottino, "Global collisional gyrokinetic simulations of ITG microturbulence starting from a neoclassical equilibrium," J. Phys.: Conf. Ser. **260**(1), 012021 (2010).
[12]J. R. Cary and A. J. Brizard, "Hamiltonian theory of guiding-center motion," Rev. Mod. Phys. **81**(2), 693–738 (2009).
[13]B. F. McMillan, S. Jolliet, T. M. Tran, L. Villard, A. Bottino, and P. Angelino, "Avalanchelike bursts in global gyrokinetic simulations," Phys. Plasmas **16**(2), 022310 (2009).
[14]Y. Sarazin, V. Grandgirard, J. Abiteboul, S. Allfrey, X. Garbet, P. Ghendrih, G. Latu, A. Strugarek, and G. Dif-Pradalier, "Large scale dynamics in flux driven gyrokinetic turbulence," Nucl. Fusion **50**(5), 054004 (2010).
[15]Z. Lin, S. Ethier, T. S. Hahm, and W. M. Tang, "Size scaling of turbulent transport in magnetically confined plasmas," Phys. Rev. Lett. **88**(19), 195004 (2002).
[16]T. S. Hahm, M. A. Beer, Z. Lin, G. W. Hammett, W. W. Lee, and W. M. Tang, "Shearing rate of time-dependent E×B flow," Phys. Plasmas **6**(3), 922–926 (1999).
[17]G. Dif-Pradalier, G. Hornung, X. Garbet, P. Ghendrih, V. Grandgirard, G. Latu, and Y. Sarazin, "The E×B staircase of magnetised plasmas," Nucl. Fusion **57**(6), 066026 (2017).
[18]Y. Idomura, H. Urano, N. Aiba, and S. Tokuda, "Study of ion turbulent transport and profile formations using global gyrokinetic full-*f* Vlasov simulation," Nucl. Fusion **49**(6), 065029 (2009).
[19]Y. Asahi, V. Grandgirard, Y. Idomura, X. Garbet, G. Latu, Y. Sarazin, G. Dif-Pradalier, P. Donnel, and C. Ehrlacher, "Benchmarking of flux-driven full-F gyrokinetic simulations," Phys. Plasmas **24**(10), 102515 (2017).
[20]P. Ghendrih, C. Norscini, T. Cartier-Michaud, G. Dif-Pradalier, J. Abiteboul, Y. Dong, X. Garbet, O. Gürcan, P. Hennequin, V. Grandgirard *et al.*, "Phase space structures in gyrokinetic simulations of fusion plasma turbulence," Eur. Phys. J. D **68**(10), 303 (2014).
[21]K. Miki, P. H. Diamond, Ö. D. Gürcan, G. R. Tynan, T. Estrada, L. Schmitz, and G. S. Xu, "Spatio-temporal evolution of the L→I→H transition," Phys. Plasmas **19**(9), 092306 (2012).
[22]X. Li, Z. Guo, and P. H. Diamond, "Formation, propagation and conversion of transport barriers triggered by dynamical critical gradient in tokamak plasmas," Nucl. Fusion **64**(4), 044001 (2024).
[23]I. Holod, W. L. Zhang, Y. Xiao, and Z. Lin, "Electromagnetic formulation of global gyrokinetic particle simulation in toroidal geometry," Phys. Plasmas **16**(12), 122307 (2009).
[24]A. J. Brizard and T. S. Hahm, "Foundations of nonlinear gyrokinetic theory," Rev. Mod. Phys. **79**(2), 421–468 (2007).
[25]A. M. Dimits, G. Bateman, M. A. Beer, B. I. Cohen, W. Dorland, G. W. Hammett, C. Kim, J. E. Kinsey, M. Kotschenreuther, A. H. Kritz *et al.*, "Comparisons and physics basis of tokamak transport models and turbulence simulations," Phys. Plasmas **7**(3), 969–983 (2000).
[26]S. Wang, Z. Wang, and T. Wu, "Self-organized evolution of the internal transport barrier in ion-temperature-gradient driven gyrokinetic turbulence," Phys. Rev. Lett. **132**(6), 065106 (2024).
[27]V. Grandgirard, Y. Sarazin, X. Garbet, G. Dif-Pradalier, P. Ghendrih, N. Crouseilles, G. Latu, E. Sonnendrücker, N. Besse, and P. Bertrand, "GYSELA, a full-f global gyrokinetic semi-Lagrangian code for ITG turbulence simulations," AIP Conf. Proc. **871**(1), 100–111 (2006).
[28]S. Ku, C. S. Chang, and P. H. Diamond, "Full-f gyrokinetic particle simulation of centrally heated global ITG turbulence from magnetic axis to edge pedestal top in a realistic tokamak geometry," Nucl. Fusion **49**(11), 115021 (2009).
[29]W. H. Lin, J. Garcia, J. Q. Li, S. Mazzi, Z. J. Li, X. X. He, and X. Yu, "A self-sustaining mechanism for internal transport barrier formation in HL-2A tokamak plasmas," Nucl. Fusion **63**(12), 126048 (2023).
[30]G. S. Xu, B. N. Wan, H. Q. Wang, H. Y. Guo, H. L. Zhao, A. D. Liu, V. Naulin, P. H. Diamond, G. R. Tynan, M. Xu *et al.*, "First evidence of the role of zonal flows for the L-H transition at marginal input power in the EAST Tokamak," Phys. Rev. Lett. **107**(12), 125001 (2011).
[31]W. Wang, Y. Kishimoto, K. Imadera, J. Q. Li, and Z. X. Wang, "Statistical study for ITG turbulent transport in flux-driven tokamak plasmas based on global gyro-kinetic simulation," Nucl. Fusion **60**(6), 066010 (2020).
[32]G. Dif-Pradalier, P. H. Diamond, V. Grandgirard, Y. Sarazin, J. Abiteboul, X. Garbet, P. Ghendrih, A. Strugarek, S. Ku, and C. S. Chang, "On the validity of the local diffusive paradigm in turbulent plasma transport," Phys. Rev. E **82**(2), 025401 (2010).
[33]Z. Lin, I. Holod, L. Chen, P. H. Diamond, T. S. Hahm, and S. Ethier, "Wave-particle decorrelation and transport of anisotropic turbulence in collisionless plasmas," Phys. Rev. Lett. **99**(26), 265003 (2007).
[34]Y. Xiao and Z. Lin, "Turbulent transport of trapped-electron modes in collisionless plasmas," Phys. Rev. Lett. **103**(8), 085004 (2009).
[35]M. J. Choi, J. Kwon, L. Qi, P. H. Diamond, T. S. Hahm, H. Jhang, J. Kim, M. Leconte, H.-S. Kim, J. Kang *et al.*, "Mesoscopic transport in KSTAR plasmas: Avalanches and the E×B staircase," Plasma Phys. Controlled Fusion **66**(6), 065013 (2024).
[36]W. Wang, Y. Kishimoto, K. Imadera, J. Q. Li, and Z. X. Wang, "A mechanism for the formation and sustainment of the self-organized global profile and E×B staircase in tokamak plasmas," Nucl. Fusion **58**(5), 056005 (2018).
[37]G. Brochard, C. Liu, X. Wei, W. W. Heidbrink, Z. Lin, N. Gorelenkov, J. Bao, A. R. Polevoi, M. Schneider, S. H. Kim, S. D. Pinches, P. Liu, J. H. Nicolau, and H. Lütjens, "Saturation of fishbone instability by self-generated zonal flows in tokamak plasmas," Phys. Rev. Lett. **132**, 075101 (2024).
[38]G. Brochard, C. Liu, X. Wei, W. W. Heidbrink, Z. Lin, M. V. Falessi, F. Zonca, Z. Qiu, N. Gorelenkov, C. Chrystal *et al.*, "Saturation of fishbone instability through zonal flows driven by energetic particle transport in tokamak plasmas," Nucl. Fusion **65**(1), 016052 (2025).
[39]P. Liu, X. Wei, Z. Lin, G. Brochard, G. J. Choi, W. W. Heidbrink, J. H. Nicolau, and G. R. McKee, "Regulation of Alfvén eigenmodes by microturbulence in fusion plasmas," Phys. Rev. Lett. **128**(18), 185001 (2022).
[40]M. V. Falessi, L. Chen, Z. Qiu, and F. Zonca, "Nonlinear equilibria and transport processes in burning plasmas," New J. Phys. **25**(12), 123035 (2023).
[41]Z. Lin, W. M. Tang, and W. W. Lee, "Gyrokinetic particle simulation of neoclassical transport," Phys. Plasmas **2**(8), 2975–2988 (1995).
[42]Z. Lin, T. S. Hahm, W. W. Lee, W. M. Tang, and P. H. Diamond, "Effects of collisional zonal flow damping on turbulent transport," Phys. Rev. Lett. **83**(18), 3645–3648 (1999).
[43]P. H. Diamond, Y.-M. Liang, B. A. Carreras, and P. W. Terry, "Self-regulating shear flow turbulence: A paradigm for the L to H transition," Phys. Rev. Lett. **72**(16), 2565–2568 (1994).
[44]H. Chen (2006). "Electrostatic full-f gyrokinetic simulation of microturbulence in tokamak using canonical Maxwellian distribution," Zenodo (ITG paper data). https://zenodo.org/records/23447453

03 November 2026 18:38:41

© Author(s) 2026